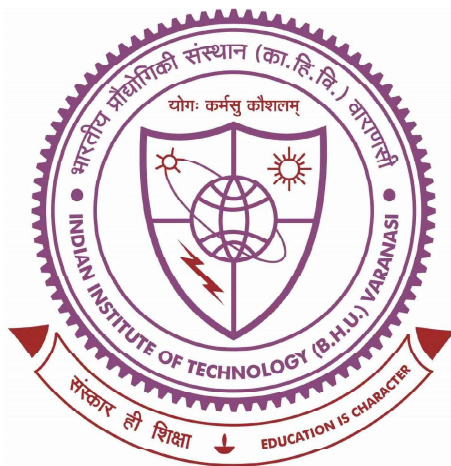


Structural, Magnetic, and Magneto-Transport Properties of Ni–Mn–In based Shape Memory Heusler Alloys and Related Systems



Thesis submitted in partial fulfilment

for the Award of

DOCTOR OF PHILOSOPHY

in

MATERIALS SCIENCE

by

KRISHNA KANT DUBEY

SCHOOL OF MATERIALS SCIENCE AND TECHNOLOGY

INDIAN INSTITUTE OF TECHNOLOGY

(BANARAS HINDU UNIVERSITY)

VARANASI – 221 005


ROLL NUMBER
18111003

YEAR OF SUBMISSION
2025

CERTIFICATE

It is certified that the work contained in the thesis titled **Structural, Magnetic, and Magneto-Transport Properties of Ni–Mn–In based Shape Memory Heusler Alloys and Related Systems** by **Krishna Kant Dubey** has been carried out under my/our supervision and that this work has not been submitted elsewhere for a degree.

It is further certified that the student has fulfilled all the requirements of Comprehensive Examination, Candidacy and SOTA for the award of **Doctor of Philosophy**.



Supervisor

Dr. Sanjay Singh

School of Materials Science and Technology

Indian Institute Of Technology

(Banaras Hindu University)

Varanasi – 221 005

Associate Professor /सह-प्राचार्य

School of Material Sciecn & Technology /पदार्थ विज्ञान एवं प्रौद्योगिकी स्कूल

Indian Institute of Technology /भारतीय प्रौद्योगिकी संस्थान

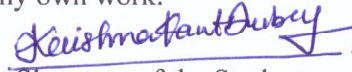
(Banaras Hindu University), Varanasi /कसी हिन्दू विश्वविद्यालय, वाराणसी

DECLARATION BY THE CANDIDATE

I, **Krishna Kant Dubey**, certify that the work embodied in this thesis is my own bonafide work and carried out by me under the supervision of **Dr. Sanjay Singh** from **July 2018** to **January 2025**, at the **School of Materials Science and Technology**, Indian Institute of Technology (Banaras Hindu University), Varanasi. The matter embodied in this thesis has not been submitted for the award of any other degree/diploma. I declare that I have faithfully acknowledged and given credits to the research workers wherever their works have been cited in my work in this thesis. I further declare that I have not willfully copied any other's work, paragraphs, text, data, results, *etc.*, reported in journals, books, magazines, reports, dissertations, theses, *etc.*, or available at websites and have not included them in this thesis and have not cited as my own work.

Date: February 19, 2025

Place: Varanasi, India


Signature of the Student

CERTIFICATE BY THE SUPERVISOR

It is certified that the above statement made by the student is correct to the best of my/our knowledge.



Supervisor

Dr. Sanjay Singh

School of Materials Science and Technology

Indian Institute Of Technology

(Banaras Hindu University)

Varanasi – 221 005

Associate Professor/सह-प्राचार्य

School of Material Sciecn & Technology /पदार्थ विज्ञान एवं प्रौद्योगिकी स्कूल

Indian Institute of Technology /भारतीय प्रौद्योगिकी संस्थान

(Banaras Hindu University), Varanasi /कशी हिन्दू विश्वविद्यालय, वाराणसी



Signature of Head of Department

Coordinator/समन्वयक

School of Materials Science & Technology/पदार्थ विज्ञान एवं प्रौद्योगिकी स्कूल

Indian Institute of Technology/भारतीय प्रौद्योगिकी संस्थान

(Banaras Hindu University), Varanasi/कशी हिन्दू विश्वविद्यालय, वाराणसी

COPYRIGHT TRANSFER CERTIFICATE

Title of the Thesis: Structural, Magnetic, and Magneto-Transport Properties of Ni–Mn–In based Shape Memory Heusler Alloys and Related Systems

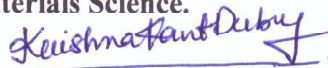
Name of the Student: Krishna Kant Dubey

COPYRIGHT TRANSFER

The undersigned hereby assigns to the Indian Institute of Technology (Banaras Hindu University), Varanasi all rights under copyright that may exist in and for the above thesis submitted for the award of the Doctor of Philosophy in Materials Science.

Date: February 19, 2025

Place: Varanasi, India


Signature of the Student

Note: However, the author may reproduce or authorize others to reproduce material extracted verbatim from the thesis or derivative of the thesis for author's personal use provided that the source and the Institute's copyright notice are indicated.

Acknowledgement

I would like to extend my deepest gratitude to my supervisor, Dr. Sanjay Singh, for his unwavering support, mentorship, and encouragement throughout my Ph.D. journey. His invaluable guidance and expertise have been pivotal in shaping my research and helping me overcome numerous challenges during this process. Dr. Singh's profound insights, constructive feedback, and thoughtful suggestions have significantly enhanced the quality and depth of my work. His patience, dedication, and belief in my abilities have inspired me to strive for excellence, and I am truly fortunate to have had the opportunity to learn under his guidance.

I am deeply grateful to Prof. Dhananjai Pandey (former institute professor at SMST) for his invaluable advice during numerous scientific discussions, as well as for his encouragement and motivation throughout my research activities. I am indebted to his expertise, dedication, and belief in my potential.

I wish to express my heartfelt appreciation to my collaborators: Prof. Claudia Felser (Max Planck Institute for Chemical Physics of Solids, Dresden, Germany), Dr. Bobby Joseph (Xpress Beamline, Elettra, Trieste, Italy), Dr. Rajeev Rawat (UGC-DAE-CSR, Indore, India), Dr. Sunil Wilfred D'Souza (University of West Bohemia, Pilsen, Czech Republic), Dr. Parul Devi (High Magnetic Field Laboratory, Dresden, Germany), Dr. Satadeep Bhattacharjee (IKST, Bangalore), Dr. Ajit Jena (IKST, Bangalore), Late Dr. P. K. Biswas (Neutron and Muon Source, ISIS, UK), Dr. Seung-Cheol Lee (IKST, Bangalore, India), Dr. Rajib Sarkar (Institute for Solid State and Materials Physics, Technical University of Dresden, Germany), Dr. C. Salazar Mejía (Max Planck Institute for Chemical Physics of Solids, Dresden, Germany), Dr. F. C. Coomer (Afton Chemical Ltd., Bracknell, Reading, UK), Dr. Dmitry A. Sokolov, and Dr. Luana Caron (Max Planck Institute for Chemical

Physics of Solids, Dresden, Germany). Their contributions, including experimental data, theoretical support, and meaningful discussions, have been instrumental in advancing my research.

I am immensely thankful to the members of my research progress evaluation committee, Dr. Shrawan Kumar Mishra and Dr. Mohammad Imteyaz Ahmad, for their invaluable guidance and diligent oversight of my research progress.

I would also like to express my sincere thanks to the faculty of SMST: Prof. Rajiv Prakash, Prof. Pralay Maiti, Prof. Chandana Rath, Prof. Akhilesh Kumar Singh, Dr. Chandan Upadhyay, Dr. Bhola Nath Pal, Dr. Ashish Kumar Mishra, Dr. Nikhil Kumar, Dr. Ravi Panwar, Dr. Uday Shankar, Dr. Shri Ram Singh (Ex-Visiting Professor), and Prof. Jitendra Kumar (Ex-Visiting Professor) for their teaching, motivation, and unwavering support.

I also thank Dr. Martin Etter and other beamline scientists at the P02.1 beamline, PETRA-III, DESY, Germany; Dr. Fabio Orlandy and other beamline scientists at the Neutron and Muon Source, ISIS, UK; and Dr. Ola Gjonnes and other beamline scientists at the high-resolution powder diffraction beamline, ESRF, France; Dr. Irshad K. A. at Xpress Beamline, Elettra, Trieste, Italy for their support and assistance.

I extend my heartfelt thanks to my seniors, Dr. Arun Kumar, Dr. Keshav Kumar, Mrs. Pragya Singh, and Dr. Anupam Kumar Singh, and my colleagues, especially Dr. Nisha Shahi, Dr. Gaurav Kumar Shukla, Mr. Vishal Kumar, Mr. Benugopal Bairagya, Ms. Shivani Rastogi, Mr. Pankaj Kumar, Ms. Nidhi Chhiller, as well as my labmates Mr. Sebananda Bhaina, Mr. Shubham Jaiswal, Ms. Aachal, Ms. Payal, Mr. Eeshan, Mr. Ujjwal, Mr. Akash, Mr. Vipul, Ms. Shivani and others, for their constant support and motivation. I also wish to thank my batchmates, friends, and fellow scholars from SMST and other departments for their encouragement. I extend my gratitude to Dr. Mohit, Dr. Satish, and Mr. Suman Karmakar from UGC-DAE-CSR, Indore, India.

I am thankful to the Department of Science and Technology, Government of India, for providing financial support to carry out synchrotron X-ray diffraction (XRD) measurements at the P02.1 beamline at PETRA-III, DESY, Germany, and pressure-dependent XRD measurements at the Xpress beamline at Elettra, Italy. I acknowledge IIT (BHU), Varanasi, and the Department of Science and Technology for supporting me through the INSPIRE fellowship scheme.

I am grateful to the Central Instrument Facility and workshops at IIT (BHU) for their assistance with various sample characterizations. I also thank the technical and non-technical staff of our department for their consistent support.

I am deeply indebted to my grandparents, parents, teachers, guardians, family members, and friends for their continuous encouragement and unconditional support. Finally, I thank Baba Vishwanath Ji, Ganga Ji, and Pt. Madan Mohan Malviya Ji for their blessings. My heartfelt gratitude extends to everyone who contributed, directly or indirectly, to the success of this thesis.

List of Figures

1.1	Phase transformations in shape memory alloy (SMA) [32].	4
1.2	A schematic diagram of face-centered cubic (FCC) austenite to body-centered tetragonal (BCT) martensite transformation via Bain distortion [41].	6
1.3	The diagram schematically illustrates the need for lattice invariant shear during martensite transformation: (a) shows the shape change during the transformation, while (b) and (c) depict how strain is accommodated by introducing slip (b) or twinning (c), respectively [41].	7
1.4	Schematic illustration of the free energy curves for both the parent (p) and martensite (m) phases [46].	8
1.5	A schematic diagram illustrating the magnetic shape memory effect: (a) shows the martensite twin reorientation in the absence of a magnetic field (twinned martensite); (b) depicts the twin reorientation in the presence of a magnetic field with weak magnetocrystalline anisotropy; (c) shows the twin reorientation under a magnetic field with strong magnetocrystalline anisotropy (detwinned martensite); (d) represents the magnetocrystalline anisotropy; and (e) illustrates the difference in Zeeman energy between the austenite and martensite phases, which is responsible for the magnetic field-induced phase transformation (MFIPT) [54].	10
1.6	Periodic table of elements: A wide range of Heusler compounds can be formed by combining elements according to the color-coded scheme [57].	12

1.7	(a) Three interpenetrating face-centered cubic (FCC) sublattices. (b) The unit cell of half Heusler compound. (c) Four interpenetrating face-centered cubic (FCC) sublattices. (d) The unit cell of the full Heusler compound.	13
1.8	A schematic representation of magnetocaloric effect.	14
1.9	Comparison of the efficiency of various caloric materials (magnetocaloric, electrocaloric, and mechanocaloric) [5].	16
1.10	Illustration of magnetocaloric effect. It represents the total entropy change as a function of entropy change and adiabatic temperature change (ΔT_{ad}) when magnetic field changes from H_0 to H_1 [72].	17
1.11	(a) Magnetization as a function of temperature [$M(T)$] at a constant field (H) (a) demonstrating conventional caloric effect. (b) demonstrating inverse caloric effect.	21
1.12	A schematic illustration of the four stages of the magnetic refrigeration cycle.	24
1.13	(a) Schematic diagram of Hall effect. (b) A typical Hall resistivity (ρ_H) as a function of magnetic field for a nonmagnetic conductor. (c) Schematic illustration of anomalous Hall effect (AHE). (d) A typical Hall resistivity (ρ_H) curve as a function of magnetic field for a ferromagnetic conductor, where $R_S M$ is the zero-field intercept [95].	26
1.14	Schematic illustrations of (a) skew scattering and (b) side jump [94].	28
1.15	(a) Bloch Skyrmion. (b) Néel Skyrmion. (c) Antiskyrmion [131] (d) Topological Hall resistivity as a function of magnetic field. Insets show skyrmion textures within positive and negative magnetic fields [132].	31
1.16	Phase diagram of $\text{Ni}_{50}\text{Mn}_{50-x}\text{In}_x$ magnetic shape memory alloy [159].	33
2.1	(a) A real image of sample preparation setup. (b) A zoomed view of the arc melting furnace.	66
2.2	X-ray diffraction by the crystal planes of a crystal	67
2.3	(a) A real image of Rigaku X-ray diffractometer (at the School of Materials Science and Technology). (b) A zoomed view of the diffractometer.	68

2.4	A schematic diagram of the synchrotron X-ray source and beamline [11].	69
2.5	(a) An illustration of optics of the beamlines at PETRA-III. [11]. (b) A real image of the P02.1 beamline station.	71
2.6	(a) A schematic diagram of the synchrotron radiation source and beamlines at Elettra. (b) Schematic diagram of diamond anvil cell (DAC). Figs. (c,d) show the real image of the experimental hutch and detector at the Xpress beamline.	72
2.7	Operation of the vibrating sample magnetometer (VSM) within a superconducting solenoid [17].	73
2.8	(a) A typical schematic diagram of four probe connections for longitudinal resistivity measurement. (b) A real image of a sample mounted on puck for the longitudinal resistivity measurement.	75
2.9	(a) A typical schematic diagram of four probe connections for transverse resistivity measurement. (b) A real image of a sample mounted on puck for the transverse resistivity measurement.	75
2.10	Sensitivity range of different experimental techniques [23].	77
2.11	Schematic diagram of zero field configuration in μ SR measurement [27].	78
3.1	(a) Typical solid-state caloric energy conversion and its advantages compared with traditional vapour-compression technique [8]. (b) Research publications for different caloric effects from 2000 to 2024 (data taken from scopus journal).	87
3.2	(a) Real image of the prototype. (b) Real image of the sample holder. Insets show a magnified view of the Gd sample with the sensor.	89
3.3	Real image of the MCE measurement set up. Inset shows a zoomed view of the sample space in the bore of the electromagnet.	90
3.4	Real image of the sample holder. Inset shows the zoomed view of the sample and sensor inside the heater coil.	91

3.5	(a) Magnetocaloric effect measurement process. (b) Adiabatic temperature change as a function of time measured in prototype for a number of field cycles.	92
3.6	Flow chart of the measurement steps in the magnetocaloric effect measurement setup.	93
3.7	Adiabatic temperature change as a function of time measured in magnetocaloric effect measurement set up for a number of field cycle.	94
4.1	Temperature dependent magnetization curve of (a) $\text{Ni}_2\text{Mn}_{1.4}\text{In}_{0.6}$ and (b) $\text{Ni}_{1.9}\text{Pt}_{0.1}\text{Mn}_{1.4}\text{In}_{0.6}$ at $H = 0.05$ T. Insets show differential ($\frac{dM}{dT}$) curves for better presentation of transition and hysteresis.	103
4.2	Le Bail refinement of SXRPD data of $\text{Ni}_{1.9}\text{Pt}_{0.1}\text{Mn}_{1.4}\text{In}_{0.6}$ in austenite phase (350 K). The experimental peak profile, calculated peak profile and the difference are shown by black circle, red and green solid lines, respectively. The blue lines represent the Bragg's peak positions.	105
4.3	Le Bail refinements of SXRPD data of $\text{Ni}_{1.9}\text{Pt}_{0.1}\text{Mn}_{1.4}\text{In}_{0.6}$ in the martensite phase at 110 K using (a) Monoclinic 3M modulated structure (space group: $I_{2/m}$) (b) Monoclinic 5M modulated structure (space group: $I_{2/m}$) (c) Monoclinic 3M modulated structure (space group: $P_{2/m}$). The experimental peak profile, calculated peak profile and difference are shown by black circle, red and green solid line, respectively. The blue lines represent the Bragg's peak positions. In the insets of (a) and (b), arrows indicate the unindexed peak. In the inset of (c), arrows show the indexed peak which were unindexed in the inset of (a) and (b).	107
4.4	Magnetization measurement results for the $\text{Ni}_{1.9}\text{Pt}_{0.1}\text{Mn}_{1.4}\text{In}_{0.6}$ (a) magnetic isotherms obtained from isothermal measurement protocol. (b) magnetic isotherms obtained from the loop measurement protocol. (c) isofield ($M(T)$) curves of $\text{Ni}_{1.9}\text{Pt}_{0.1}\text{Mn}_{1.4}\text{In}_{0.6}$ at different field values. (d) magnetic isotherms extracted from isofield curves shown in (c).	110

4.5	Comparison of isothermal entropy change ΔS_{iso} as a function of temperature for the isofield, isothermal, and loop measurement protocols for $\text{Ni}_{1.9}\text{Pt}_{0.1}\text{Mn}_{1.4}\text{In}_{0.6}$ at different applied field values (a) 1 T (b) 3 T (c) 4 T and (d) 7 T.	111
5.1	Magnetization as a function of temperature ($M(T)$) for zero-field cooling (ZFC), field-cooled cooling (FCC), and field-cooled heating (FCW) with a 500 Oe external magnetic field. Inset (i) magnified view of the $M(T)$ plot around T_C . (ii) magnified view of $1/\chi$ vs T plot at high temperature [44].	128
5.2	(a and b) The muon spin relaxation data measured in zero magnetic field (ZF) at various temperatures. The dotted curve depicts the observed data, and the lines indicate the calculated data. The inset displays the asymmetry data as a function of time at 421 K.	130
5.3	(a) The muon asymmetry A_{10} measured as a function of temperature in zero magnetic field during the cooling process. (b) The temperature dependence of the muon depolarization rate λ measured in zero magnetic field during cooling.	132
5.4	(a) Synchrotron X-ray powder diffraction (SXRPD) patterns of $\text{Ni}_2\text{Mn}_{1.4}\text{In}_{0.6}$ are shown at representative temperatures. Insets show a magnified view of the most intense peak at their respective temperatures (b) Le Bail refinement of the SXRPD pattern of $\text{Ni}_2\text{Mn}_{1.4}\text{In}_{0.6}$ in the austenite phase at 350 K. Inset (i) shows a magnified view of the (111) and (200) peaks, indicating $L2_1$ ordering. Inset (ii) shows the fitted most intense peak (220). (c) Le Bail refinement of SXRPD pattern of $\text{Ni}_2\text{Mn}_{1.4}\text{In}_{0.6}$ in the martensite phase at 250 K. The inset displays an enlarged view of the split main peak. The experimental peak profile is represented by black circles, while the calculated peak profile and the difference are shown by the red and green solid lines, respectively. The blue lines mark the positions of the Bragg peaks.	134

- 5.5 Real space Rietveld refinement of PDF data using space group $Fm\bar{3}m$ (a) at 350 K (b) at 300 K in long-range. Black dots represent the observed data points, the orange line indicates the calculated data points, and the green line indicates the difference between the observed and calculated data. The insets provide a zoomed view of the misfit peaks. (c) Temperature-dependent PDF data are plotted as a function of atomic pair distance in the temperature range 350 K to 120 K at representative temperatures. Insets show a zoomed view around the expected newly developed martensite peaks. (d) Real space Rietveld refined PDF data at 120 K using space group $P_{2/m}$ modulated structure. 135
- 5.6 Figs (a) & (b) show the real space Rietveld double phase refined PDF data using space group $Fm\bar{3}m$ and $P_{2/m}$ at 350 K and 300 K in LR. Insets show the zoomed view of the unfitted peaks at 3.32 Å and 3.85 Å. Figs (c) & (d) show the real space Rietveld double phase refined PDF data using space group $Fm\bar{3}m$ and $P_{2/m}$ at 350 K and 300 K in SR. Insets show the zoomed view of the fitted peaks at 3.32 Å and 3.85 Å. Black dots represent the observed data points, the orange line indicates the calculated data points, and The green line indicates the difference between the observed and fitted plots 137
- 6.1 Le Bail refinement of synchrotron X-ray powder diffraction (SXRPD) data of $\text{Ni}_{50}\text{Mn}_{34}\text{In}_{15.2}\text{Al}_{0.8}$ MSMA at 300 K. The experimental peak profile, calculated peak profile and the difference are shown by black solid circle, red and blue lines, respectively. The green lines represent the Bragg's peak positions. The inset presents a zoomed view of the (111) and (200) superlattice peaks. 156

- 6.2 (a) Temperature-dependent magnetization plot $M(T)$ of, $\text{Ni}_{50}\text{Mn}_{34}\text{In}_{15.2}\text{Al}_{0.8}$ MSMA at 500 Oe. The inset shows the zoomed view of $M(T)$ near the cubic to PM-phase transition temperature. (b) Temperature-dependent longitudinal resistivity (ρ_{xx}) at zero field. (c) Magnetic field-dependent magnetization [$M(H)$] at representative temperatures. Inset shows the saturation magnetization. (d) magnetic field dependent percentage magnetoresistance [MR(%)] at representative temperatures. 157
- 6.3 (a) Total Hall resistivity (ρ_H) as a function of magnetic field at the specified temperatures. (b) Anomalous Hall coefficient (ρ_{AH}/M_s). Inset shows the anomalous Hall conductivity. (c) Temperature dependence of the normal Hall coefficient (R_0). Inset displays the variation of carrier concentration n with temperature. (d) The logarithmic plot of ρ_{AH}/M_s vs ρ_{xx} (blue solid circles) with a linear fit is shown by the red line. The inset presents the plot between ρ_{AH}/M_s and ρ_{xx} (black solid circles). 159
- 6.4 The total Hall resistivity (black colour), calculated Hall resistivity (red colour), and extracted topological Hall resistivity (blue colour) curves are shown as a function of magnetic field at (a) 350 K (b) 300 K (c) 275 K (d) 200 K. (e) shows the extracted topological Hall resistivity (ρ^T) at the representative temperatures. Inset depicts the $\rho^T(\text{max})$ as function of temperature. (f) Contour plot of the magnitude of ρ^T 160
- 7.1 Le Bail fit of room temperature SXRPD pattern. Black dots, red and green solid lines, respectively, show the experimental data, calculated data and the residue. The blue ticks represent Bragg's peak positions. 177
- 7.2 Zero field cooled magnetization measurement as a function of the temperature at low field (100 Oe) [65]. Magnetic states are highlighted with distinct colours. " T_C " represents the Curie temperature. Inset shows a magnified view of the plot around the thermodynamically stable skyrmions regime. 178

- 7.3 (a) Pressure-dependent SXRPD patterns with increasing pressure at room temperature. A pattern was also recorded during pressure release at 2.5 GPa. (b) Lattice parameters as a function of pressure along the a axis, i.e. in plane and (c) along the c axis, i.e. out of plane. The continuous red line represents the linear fitting, and the dotted blue line represents an extrapolated line, respectively. The slope of the line indicates the unit-cell parameter reduction rate with pressure. Magenta colour points correspond to the lattice parameter after pressure release at 2.5 GPa. The error in unit-cell parameters is smaller than the symbol size used for representation. 179
- 7.4 (a) Unit-cell volume as a function of pressure. Black dots represent the experimental data. Red and blue solid lines indicate the results of fitted data using B–M EoS above ~ 6 GPa (“EoS1”) and below the ~ 6 GPa pressure (“EoS2”) regime. A magenta colour point corresponds to the volume at 2.5 GPa after pressure release. (b) Reduced pressure (H) versus Eulerian strain (f_E) curve. Inset shows the c/a ratio as a function of pressure. 180
- 7.5 (a) The Evolution of SXRPD data as a function of the temperature from 150 to 300 K of PtMnGa system. Inset shows the magnified view of the peak shift around main Bragg’s peak regime. (b) and (c) Le Bail fit of SXRPD data at 300 K [65] and 150 K, respectively. Black dots, red and green solid lines, respectively, show the experimental data, calculated data and the residue. The blue ticks represent Bragg’s peak positions. 182
- 7.6 (a) $a/a_{300 K}$ as a function of temperature along the a axis, i.e. in plane. (b) $c/c_{300 K}$ as a function of temperature along the c axis, i.e. out of plane. (c) Volume as a function of temperature. The continuous red line represents the linear fitting. The error in unit-cell parameters is smaller than the symbol size used for representation. 183

7.7	Electronic band structure at different representative pressures of the hexagonal PtMnGa in both the spin channels (majority and minority). The up and down arrows represent the spin majority and minority electrons, respectively. The regions where the red-coloured dotted rectangles highlight the degenerate bands.	184
7.8	(a) The density of states at the Fermi level (Fermi energy set to zero) versus pressure curve for two spin channels. (b) shows the magnetic moment per formula unit. The red solid lines represent the linear fit.	186
7.9	Field-dependent magnetization ($M(H)$) data of PtMnGa, measured at $T = 250$ K under 0 GPa and 0.6 GPa pressure. Inset shows the zoomed view of ($M(H)$) plot at higher field regime.	189
7.10	Fitting to the law of approach to saturation of [$M(H)$] data measured at 250 K (a) under 0 GPa pressure (b) 0.6 GPa pressure.	190
7.11	$M_S(T)/M_S(0)$ as a function of the $T^{(3/2)}$ and red line shows the fitted data at 7 T field.	191
7.12	Micromagnetic simulation results for (a) 0 GPa, 250 K and 0.25 T (b) 0 GPa, 250 K and 0.25 T (c) and (d) calculation of topological charge. . . .	193

List of Tables

5.1	Lattice parameters obtained from the PDF refinement using cubic phase with space group $Fm\bar{3}m$ and monoclinic phase with space group $P_{2/m}$ with 3M modulation in the LR regime at 350 K and 300 K.	139
5.2	Lattice parameters obtained from the PDF refinement using cubic phase with space group $Fm\bar{3}m$ and monoclinic phase with space group $P_{2/m}$ with 3M modulation in the SR regime at 350 K and 300 K.	140
7.1	Comparison of temperature and pressure dependent lattice parameters (a and c) of hexagonal PtMnGa.	194